Journal of Intelligent & Robotic Systems (2021) 103: 9
https://doi.org/10.1007/s10846-021-01436-9

SHORT PAPER

Multibody-Dynamic Modeling and Stability Analysis for a Bird-scale Flapping-wing Aerial Vehicle

Yaolei Shen[1] · Wenjie Ge[1] · Pu Miao[1]

Received: 15 December 2020 / Accepted: 9 June 2021 / Published online: 6 August 2021

Abstract

In this work, we present a new mathematic model for the flight of a bird-scale flapping-wing aerial vehicle, in which the impacts of the wing inertia and its deformations are considered. Based on this model, the longitudinal and later-directional orbit stability of the vehicle at uncontrolled condition are proved to be steady via Floquet Theory combined with the untethered flight experiment. However, both simulation and experiment show that the vehicle presents a periodical motion state which is similar to spiral flight at uncontrolled condition. At this spiral-like flight state, the yaw angle of the vehicle varies constantly, which makes it difficult to meet the requirements of the general flight mission. In this case, two independent PID controllers are designed to stabilize the vehicle attitude based on the approximate linear model in the vicinity of the equilibrium flight condition. And the controlled flight of the vehicle prototype is also proved to be stable through numerical calculation and physical experiment.

Keywords Flapping-wing flight · Aerial robotics · Dynamic modelling · Stability analysis

1 Introduction

Bird, bat and insect flight has fascinated humans for many centuries [1]. Especially in these two decades, with the developing investigation in human-engineered flapping-wing-based aerial vehicles, many excellent insect-scale flapping-wing aerial vehicles [2–4] and bird-scale flapping-wing aerial vehicles [5–7] have realized controlled flight, which definitely revolutionize our capabilities in areas such as environment monitoring and surveillance and security [8].

Compared with conventional fixed wing aircrafts and rotor-based aircrafts which use the rotantional motion of propellers to realize flight [9, 10], flapping-wing aerial vehicles can generate both thrust and lift to maintain flight through flapping wing motions. However, the complex flight mechanism of flapping-wing vehicles dramatically increases the difficulty in dynamic modelling [11] and aerodynamic analysis [12] of the flapping wing flight. In this topic, some literatures derived the motion equations of the flapping-wing vehicle flight based on standard aircraft model and quasi-steady aerodynamic model, in which the inertial effects of the wings are neglected [13–15]. In order to improve the precision of modelling, Lasek and Sibilski and Buler et al. derived the multi-body dynamic model of the flapping-wing aerial vehicle via Gibbs-Appel Equation, in their model the wing motions are limited to two degrees of freedom: flapping and lagging [16]. Besides, in [17], Grauer and Hubbard derived the motion equations of an ornithopter using the Boltzman–Hamel Equations and five rigid bodies: one for the central body, one for each wing, and two determining the linkage for the tail. Orlowski et al. derived the equations of motion for a flapping wing micro-air vehicle using D'Alembert's Principle for Multiple Rigid Bodies, and in their model the wings are determined by three degrees of freedom [18]. In addition to mechanism-based modeling, Pfeiffer and Lee and Han et al. realized the flight simulation of flapping-wing vehicle via the co-simulation of MSC. ADAMS and ANSYS, in which the deformations of the wings can be also simulated by fluid-structure interaction method [19].

✉ Wenjie Ge
gwj@nwpu.edu.cn

Yaolei Shen
yaolei_shen@mail.nwpu.edu.cn

Pu Miao
sxlf@mail.nwpu.edu.cn

[1] School of Mechanical Engineering, Northwestern Polytechnical University, Xi'an 710072, China

The investigation of flight modeling of flapping-wing aerial vehicle naturally leads to its stability analysis, which is significant to the design of aircraft. Taylor and Thomas firstly analyzed the dynamic stability of the desert locust Schistocerca gregaria in [20], in which the mass of the wings is neglected due to the assumption that the wings beat fast enough to not excite the rigid body modes of the central body. In [21], Sun and Xiong used the same approximation to analyze the hovering flight stability of a bumblebee. In their work, the aerodynamic forces and moments are cycle-averaged, and the resultant forces over one flapping cycle are used to determine the equilibrium flight condition in the vicinity of a hover condition [21]. The analysis results show that, based on the linearized system, the bumblebee flight is unstable at the longitudinal axis [21]. After that, Bolender analyzed the orbital stability for the hover motion of flapping-wing micro air vehicle via Floquet Theory, the analysis results show the system has unstable orbits [22]. Dietl and Garcia also used Floquet Theory to analyze the longitudinal orbital stability for the forward flight condition of an ornithopter, and lead to the unstable conclusion [23]. However, in their work [23], the passive deformation angles of the wings are set beforehand, which may induce differences to the dynamics of the physical counterpart. In addition, Kim and Lee and Han used the co-simulation method of MSC. ADAMS and ANSYS to analyze the longitudinal orbital stability for an ornithopter, the analysis results show that the passive deformations of the wings will increase the stability of flapping wing flight [24]. Besides, they found that the increase of flapping wing frequency leads to the decrease of vibration amplitude at pitch angle [25]. Furthermore, Stanford and Beran and Patil optimized the wing kinematics of flapping-wing vehicle via Floquet Theory, and realized the stabilized flight [26]. After that, Bhatia and Patil and Woolsey et al. designed a LQR controller for the model presented in [26] to adjust the wings kinematics parameters, and realized the stabilized flight of flapping-wing vehicle in gust environments [27].

In this work, the inertial effects and passive deformations effects of the wings are considered in the flapping-wing aerial vehicle flight modelling. Based on this model, the longitudinal stability and lateral-directional stability of the vehicle uncontrolled flight are analyzed respectively. After that, in order to stabilize the attitude of the flapping-wing aerial vehicle, two independent PID controllers are designed respectively in pitch angular channel and yaw angular channel according to the approximate linear model in the vicinity of the equilibrium flight condition. And the close-loop controlled flight stability of the vehicle is also analyzed.

This paper is structured as follows. Section 2 is the description of the modelling procedure of the vehicle prototype. Section 3 presents the stability analysis of the vehicle flight under uncontrolled condition and controlled condition respectively via Floquet Theory. Section 4 presents the physical prototype flight experiments including parameter identification and untethered flight tests. Section 5 summarizes the main conclusions and suggestions for futher work.

2 Mathematical Model

2.1 Description of Flapping-wing Aerial Vehicle

The flapping-wing aerial vehicle prototype in this work is shown at Fig. 1. This vehicle uses two servo motors to drive the elevator and the rudder respectively, and it uses a brushless motor to drive the flapping-wing mechanism and the two wings via a gear box. Two symmetric four-bar mechanisms coupled with two gear wheels form the flapping-wing mechanism, whose parameters are optimized with the seagull flapping wing flight kinematics data [28]. And the wing flapping motion rule is designed to be close to the second order Fourier series obtained at [28], which is shown at Eq. 1.

$$\begin{aligned}\phi(t) = \; & 8.4654 - 8.5368 \cdot sin(\omega t) + 17.8798 \cdot cos(\omega t) \\ & +1.0898 \cdot sin(2\omega t) - 4.5880 \cdot cos(2\omega t)\end{aligned} \tag{1}$$

In which, the unit of the wing flapping angle $\phi(t)$ is deg, ω is angular frequency whose unit is $\mathrm{rad} \cdot \mathrm{s}^{-1}$. And the physical parameters of the prototype are shown at Table 1.

2.2 Definition and Assumptions for the Model

During flight motion, the flapping-wing aerial vehicle can be regarded as an open kinematic chain that evolves under the influence of gravitational and external aerodynamic

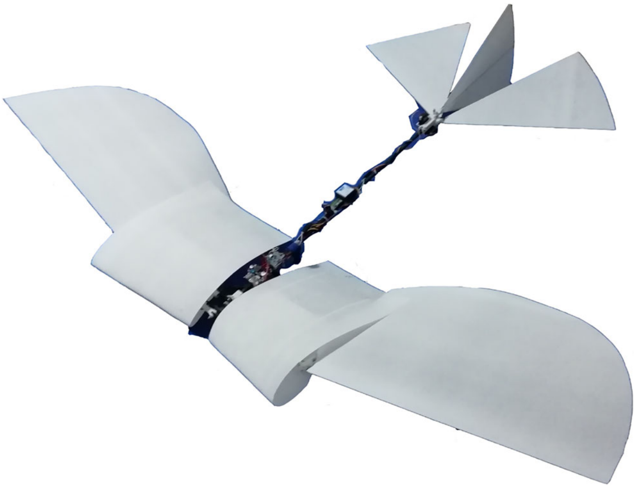

Fig. 1 Flapping-wing aerial vehicle prototype

Table 1 Physical parameters of the prototype

Wing span:	1.5 m
Body length:	1.2 m
450 mAh Li-Poly Battery:	46 g
BLDC Motor for wings:	57 g
Frame & gear box:	265 g
Two servo motors for tails:	25 g
Tail joints:	23 g
Tail fans:	26 g
Wings:	116 g
Total weight:	558 g

forces. For analyzing and controlling this evolution, it is essential to derive the mathematical model of the vehicle flight. Figure 2 shows the multi-body model of the flapping-wing aerial vehicle prototype, which consists of body, two primary wings, two secondary wings, two elevator fans and rudder fan. In this model, every two adjacent parts are connected by hinges, in which two tail joints and two shoulder joints are actuated joint, and the two elbow joints are unactuated, this means that the two primary wings will twist under the influence of inertia and forces caused by gravity and aerodynamic. These two passive elbow joints can be used to consider the effect of the deformations of the two primary wings.

The open kinematic chain of the prototype can be defined with some generalized coordinates. As shown in Fig. 2, the orientation and position of prototype body according to the inertial absolute coordinate $O_0 E_x E_y E_z$ can be defined with the body-fixed coordinate $o_B e_x e_y e_z$ located at the mass center of body. In this case, the orientation of coordinate $o_B e_x e_y e_z$ can be determined by the Euler angles (q_x, q_y, q_z), which follow the rotating order “ZYX”, and the position of body mass center o_B is defined by (p_x, p_y, p_z). The wings can be determined by two actuated joint coordinates (ϕ_R, ϕ_L) and two passive coordinates (δ_R, δ_L), and the elevators and rudder can be determined by coordinates (δ_e, δ_r) respectively.

For modeling the flight of the vehicle prototype, there are some assumptions made as preconditions:

1) The influence of the primary wing deformation on the inertia of the whole wing is neglected.
2) The mass of the tail fans is not considered.
3) The aerodynamic forces on vehicle body are not considered.
4) The aerodynamic forces on tail fans caused by the velocity of tail joints are neglected.
5) The flapping motions of two wings follow the rule shown at Eq. 1.

2.3 Rigid Multi-body Dynamics

Due to the assumption (1), the primary and secondary wings on the same side of the vehicle body can be considered as a whole, that is, as a rigid body. Besides, according to the assumption (2), the tails can be considered as parts of vehicle body during the rigid multi-body dynamic modeling. Hence, the vehicle prototype dynamic model is simplified as a three rigid body model composed of body, left wing and right wing. And the dynamic model can be determined with the generalized coordinates $q = [p_x, p_y, p_z, q_x, q_y, q_z, \phi_R, \phi_L]^T \in R^8$.

In this work, recursive Newton-Euler method is used for the formulation and solution of the simplified prototype dynamical equations to avoid complex symbolic differential

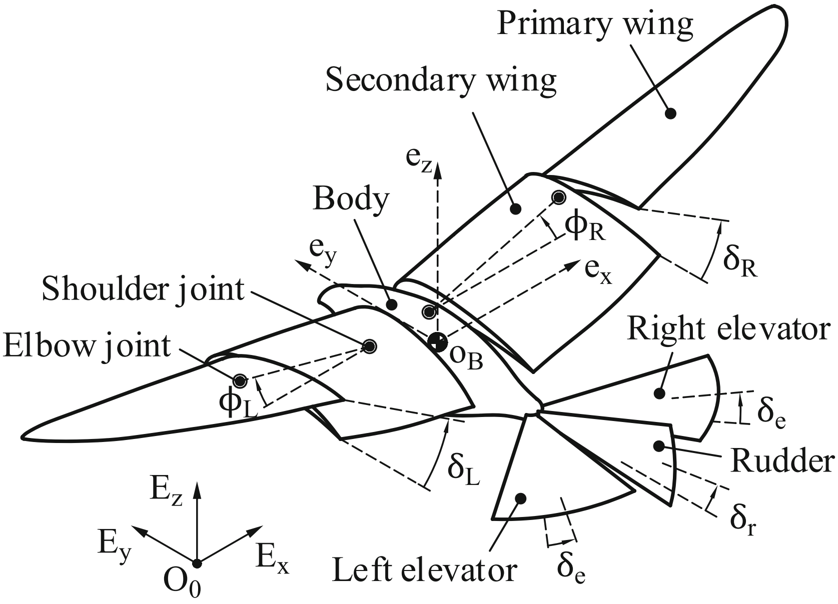

Fig. 2 Multi-body model of the vehicle prototype

procedures. This method calculates the forward dynamics of vehicle prototype with several inverse dynamic sub procedures nested. In which, the inverse dynamics procedure based on recursive Newton-Euler method includes two steps. First, the velocity and acceleration of each rigid body is calculated from the base to two wings iteratively. After that, external force and moment of each rigid body is obtained from two wings to the base iteratively. During analyzing the motion of vehicle body, it can be considered as a virtual joint located from the original point of base O_0 to the body mass center o_B which consists of three translational joint along the three axes of the inertial reference coordinate system $O_0E_xE_yE_z$ and three Euler rotational joint follow the order "ZYX", and this virtual joint can be determined by coordinates $(p_x, p_y, p_z, q_x, q_y, q_z)$. In this case, the kinematics and external force and moment of each part can be calculated iteratively via inverse dynamics Newton-Euler method (Fig. 3).

The kinematics iterative calculation is different in translational joint and rotational joint. As for translational joint:

$$\begin{aligned}
{}^{i+1}_{i+1}\omega &= {}^{i+1}_{i}R \cdot {}^{i}_{i}\omega \\
{}^{i+1}_{i+1}\dot{\omega} &= {}^{i+1}_{i}R \cdot {}^{i}_{i}\dot{\omega} \\
{}^{i+1}_{i+1}\upsilon &= \dot{q}_{i+1} \cdot {}^{i}_{i}k + {}^{i+1}_{i}R \cdot ({}^{i}_{i}\omega \times {}^{i}_{i+1}p + {}^{i}_{i}\upsilon) \\
{}^{i+1}_{i+1}\dot{\upsilon} &= \ddot{q}_{i+1} \cdot {}^{i}_{i}k + 2({}^{i+1}_{i+1}\omega \times \dot{q}_{i+1} \cdot {}^{i}_{i}k) \\
&\quad + {}^{i+1}_{i}R \cdot [{}^{i}_{i}\dot{\omega} \times {}^{i}_{i+1}p + {}^{i}_{i}\omega \times ({}^{i}_{i}\omega \times {}^{i}_{i+1}p) + {}^{i}_{i}\dot{\upsilon}]
\end{aligned} \tag{2}$$

And as for rotational joint:

$$\begin{aligned}
{}^{i+1}_{i+1}\omega &= {}^{i+1}_{i}R \cdot {}^{i}_{i}\omega + \dot{q}_{i+1} \cdot {}^{i}_{i}k \\
{}^{i+1}_{i+1}\dot{\omega} &= {}^{i+1}_{i}R \cdot {}^{i}_{i}\dot{\omega} + \ddot{q}_{i+1} \cdot {}^{i}_{i}k + {}^{i+1}_{i}R \cdot [{}^{i}_{i}\omega \times (\dot{q}_{i+1} \cdot {}^{i}_{i}k)] \\
{}^{i+1}_{i+1}\upsilon &= {}^{i+1}_{i}R \cdot ({}^{i}_{i}\omega \times {}^{i}_{i+1}p + {}^{i}_{i}\upsilon) \\
{}^{i+1}_{i+1}\dot{\upsilon} &= {}^{i+1}_{i}R \cdot [{}^{i}_{i}\dot{\omega} \times {}^{i}_{i+1}p + {}^{i}_{i}\omega \times ({}^{i}_{i}\omega \times {}^{i}_{i+1}p) + {}^{i}_{i}\dot{\upsilon}]
\end{aligned} \tag{3}$$

In which, ${}^{i}_{i}\omega$ and ${}^{i}_{i}\dot{\omega}$ are the angular velocity and angular acceleration of i^{th} rigid body in its coordination system $o_ie_xe_ye_z$ respectively, ${}^{i}_{i}\upsilon$ and ${}^{i}_{i}\dot{\upsilon}$ are the translational velocity and translational acceleration of i^{th} rigid body in its coordination system $o_ie_xe_ye_z$ respectively. ${}^{i}_{i+1}p$ is the position vector from the original point of coordination system $o_ie_xe_ye_z$ to original point of $o_{i+1}e_xe_ye_z$ in the coordination system $o_ie_xe_ye_z$. ${}^{i}_{i}k$ is the normalized vector of the motion axis of i^{th} joint in the coordination system $o_ie_xe_ye_z$. q_{i+1} is the motion coordinate of i^{th} joint, for translational joint q_{i+1} is the linear displacement, and q_{i+1} means angular displacement when i^{th} joint is rotational joint. ${}^{i+1}_{i}R$ is the transformational matrix from coordination system $o_ie_xe_ye_z$ to $o_{i+1}e_xe_ye_z$.

Then, the external force and moment at body mass center can be obtained as:

$$\begin{aligned}
{}^{i}_{i}\dot{\upsilon}_c &= {}^{i}_{i}\dot{\upsilon} + {}^{i}_{i}\dot{\omega} \times {}^{i}_{i}r_c + {}^{i}_{i}\omega \times ({}^{i}_{i}\omega \times {}^{i}_{i}r_c) \\
{}^{i}_{i}f_c &= m_i \cdot {}^{i}_{i}\dot{\upsilon}_c \\
{}^{i}_{i}n_c &= {}^{i}_{i}I_c \cdot {}^{i}_{i}\dot{\omega} + {}^{i}_{i}\omega \times ({}^{i}_{i}I_c \cdot {}^{i}_{i}\omega)
\end{aligned} \tag{4}$$

Fig. 3 Simplified model of the vehicle prototype

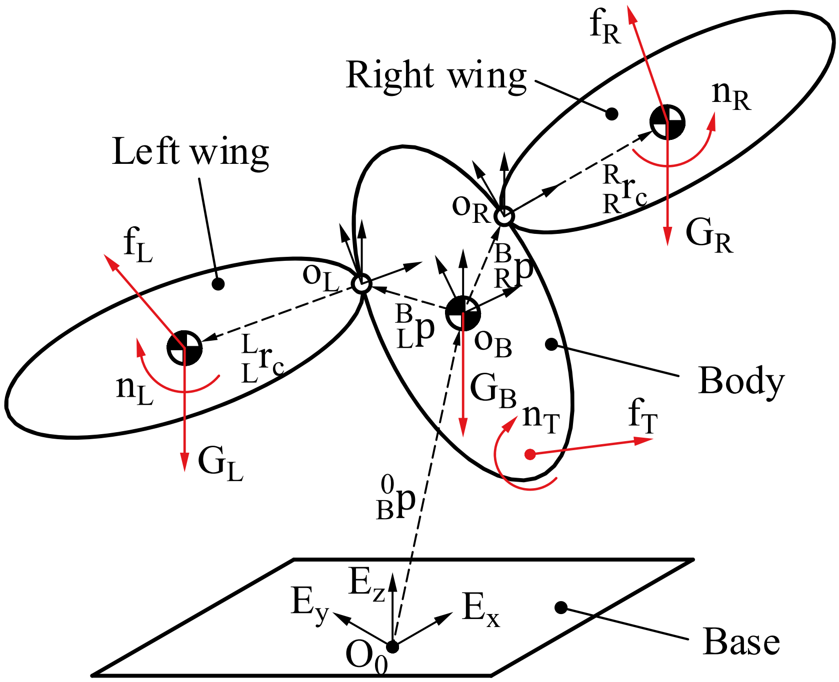

In which, ${}^i_i\dot{v}_c$ is the translational acceleration of i^{th} rigid body mass center in its coordination system $o_i e_x e_y e_z$, ${}^i_i r_c$ is the position vector of i^{th} rigid body mass center in $o_i e_x e_y e_z$. m_i and ${}^i_i I_c$ is the mass and moment inertia matrix of i^{th} rigid body respectively.

After that, the constraint force and moment of each joint can be calculated as:

$$\begin{aligned} {}^i_i f &= {}^i_i f_c + {}^i_i f_{ext} + {}^i_{i+1}R \cdot {}^{i+1}_{i+1} f \\ {}^i_i n &= {}^i_i n_c + {}^i_i n_{ext} + {}^i_{i+1}R \cdot {}^{i+1}_{i+1} n \\ &\quad + {}^i_i r_c \times ({}^i_i f_c + {}^i_i f_{ext}) + {}^i_{i+1} p \times ({}^i_{i+1}R \cdot {}^{i+1}_{i+1} f) \\ \tau_i &= {}^i_i n \cdot {}^i_i k \\ f_i &= {}^i_i f \cdot {}^i_i k \end{aligned} \tag{5}$$

In which, ${}^i_i f$ and ${}^i_i n$ are the constraint force and moment of i^{th} joint in coordination system $o_i e_x e_y e_z$. ${}^i_i f_{ext}$ and ${}^i_i n_{ext}$ are the equivalent force and moment on i^{th} rigid body mass center caused by the interaction with environment, which are aerodynamic force and moment in this work. ${}^i_{i+1}R$ is the transformational matrix from coordination system $o_{i+1} e_x e_y e_z$ to $o_i e_x e_y e_z$. τ_i is the driving torque on rotational joint, and f_i is driving force on translational joint.

During the forward dynamical solution, the equations of motion of vehicle prototype take the form as:

$$M(q)\ddot{q} + C(q,\dot{q})\dot{q} + G(q) = Q \tag{6}$$

In which, $q = [p_x, p_y, p_z, q_x, q_y, q_z, \phi_R, \phi_L]^T$ is the generalized coordinate vector of the multi rigid body system. $M(q) \in R^{8\times 8}$ is the inertia matrix, $C(q,\dot{q}) \in R^{8\times 8}$ is the Coriolis matrix, $G(q) \in R^8$ is the gravity vector and $Q \in R^8$ denotes all applied non-conservative forces. According to Eq. 6, if $\dot{q}$, ${}^i_i f_{ext}$, ${}^i_i n_{ext}$ and gravity acceleration g are set to be zero, and $\ddot{q}$ is set to be $e_j \in R^8$ whose elements are zero except its j^{th} element, which is one, then the vector composed of the driving forces of the eight joints obtained during the inverse dynamics calculation is the j^{th} column vector of $M(q)$. And if $\ddot{q}$, ${}^i_i f_{ext}$, ${}^i_i n_{ext}$ are set to be zero, then the driving forces vector is the sum of Coriolis force, centrifugal force and gravitational force, namely $C(q,\dot{q})\dot{q} + G(q)$. Finally, if $\dot{q}$ and $\ddot{q}$ are set to be zero, and gravity acceleration g are set to be zero, then the driving forces vector obtained is the generalized force Q.

2.4 Aerodynamic Model

The flight of birds, insects and others flying animals is benefited from the unsteady aerodynamic mechanism, which can be simulated based on the finite element solution of the Navier-Stokes equations [29, 30]. However, this method is hard to be applied on control purposes, since it requires several hours for simulating a single wingbeat. Fortunately, thanks to scaled models of flapping wings [31, 32], several advances have been achieved in understanding the unsteady aerodynamic mechanism.

The mathematical aerodynamic modeling method adopted in this work is based on the quasi-steady aerodynamic model, which can reduce the time of simulating the flapping-wing flight of prototype to one second for a single wingbeat. According to the quasi-steady approach, the total force on a wing is obtained by diving the wing into infinitesimal blades of thickness dr, and the force on each blade can be calculated as Eq. 7 which is similar to [33]

$$\begin{aligned} dF_L(t,r) &= \tfrac{1}{2} C_L(\alpha(t))\rho c(r) U^2(t,r) dr \\ &\quad + \tfrac{1}{2} C_{rot} \rho c^2(r) U(t,r) \dot{\alpha}(t) dr \\ dF_D(t,r) &= \tfrac{1}{2} C_D(\alpha(t))\rho c(r) U^2(t,r) dr \end{aligned} \tag{7}$$

In which, dF_L and dF_D are lift and drag of each wing blade respectively, α is the local attack angle of the wing blade, ρ is the density of air which is set to be $1.293\ \mathrm{kg \cdot m^{-3}}$ in this work, c is the chord length of the wing blade, U is the wing blade velocity relative to the fluid, C_L and C_D are lift coefficient and drag coefficient respectively. C_{rot} is the rotational force coefficient, which can expressed as $C_{rot} = 2\pi((3/4) - \hat{x}_0)$, $\hat{x}_0$ is the dimensionless distance of the longitudinal rotation axis from the leading edge, which is set to be 1/4 in this work. These parameters are illustrated in Fig. 4, in which coordinate system $ox_w y_w$ is the local wind coordinate of wing blade whose x axis is parallel to the direction of U.

Fig. 4 Aerodynamic force on wing blade

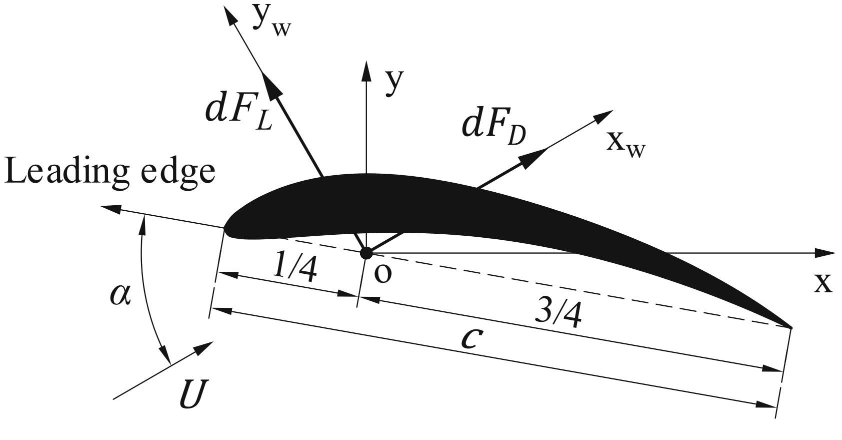

In addition, since the primary wings adopted on the vehicle prototype are thin airfoil which is similar to the wing configures in [31], the aerodynamic coefficients C_L and C_D of the primary wings are formed by the results from [31]. And its expressions are shown as follows:

$$\begin{aligned} C_L &= 0.225 + 1.58sin(2.13\alpha - 7.20) \\ C_D &= 1.92 - 1.55cos(2.04\alpha - 9.82) \end{aligned} \tag{8}$$

However, these two coefficients of the secondary wings need to be redetermined due to the different airfoil type. In this work, the C_L and C_D of the secondary wing blade is adopted by the corresponding static aerodynamic coefficients which are obtained from the CFD simulating. And the expressions of these two coefficients are shown as follows:

$$\begin{aligned} C_L = {} & 1.125sin(1.04\alpha + 1.325) \\ & +1.126sin(2.056\alpha + 0.06919) \\ C_D = {} & 5.096sin(0.02086\alpha + 0.2175) \\ & +1.087sin(1.945\alpha - 1.505) \end{aligned} \tag{9}$$

Figure 5 shows the original data and the fitting expressions of the aerodynamic coefficients of secondary wings. Compared with the results in [31], it can be found that the lift coefficient C_L of secondary wings is larger than that of primary wing when the local attack angle of airfoil blade is between -60° and 60°. When the local attack angle locates in the range from 60° to 120°, the lift coefficients in primary and secondary wings are approximately equal. And when local attack angle locates in the range from -180° to -60° or the range from 120° to 180°, the lift coefficient of primary wings becomes lager than that of secondary wings. Besides, the variation trend of the drag coefficient of the secondary wings according to the attack angle is similar to that of the primary wings, while the value of the coefficient of seconding wings is smaller than that in primary wings.

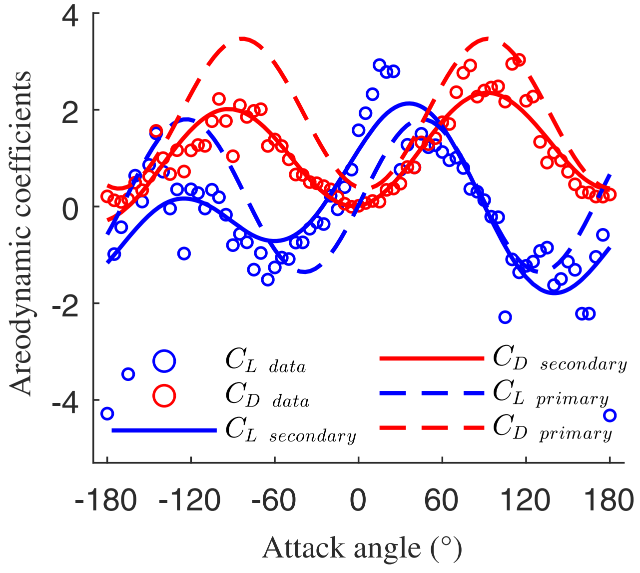

Fig. 5 Aerodynamic coefficients of wings

From Eqs. 7–9, the force and moment of each blade of primary wing and secondary wing on the mass center of the whole wing can be obtained in the shoulder joint coordinate system $o_s e_x e_y e_z$. After deriving the sum of these forces and moments, the aerodynamic force and moment on the wing mass center can be calculated as follow:

$$\begin{aligned} {}^s_s f_{ext} = {} & \sum {}^s_i R \cdot \begin{bmatrix} 0 \\ -dF_D(t,r)_i \\ dF_L(t,r)_i \end{bmatrix} \\ & + \sum {}^s_e R \cdot {}^e_j R \cdot \begin{bmatrix} 0 \\ -dF_D(t,r)_j \\ dF_L(t,r)_j \end{bmatrix} \\ {}^s_s n_{ext} = {} & \sum ({}^s_s r_i - {}^s_s r_c) \times \left({}^s_i R \cdot \begin{bmatrix} 0 \\ -dF_D(t,r)_i \\ dF_L(t,r)_i \end{bmatrix} \right) \\ & + \sum ({}^s_s r_j - {}^s_s r_c) \times \left({}^s_e R \cdot {}^e_j R \cdot \begin{bmatrix} 0 \\ -dF_D(t,r)_j \\ dF_L(t,r)_j \end{bmatrix} \right) \end{aligned} \tag{10}$$

In which, ${}^s_i R$ is the rotational transformation matrix from the shoulder joint coordinate system $o_s e_x e_y e_z$ to the local wind coordinate system $o_i e_x e_y e_z$ on the quarter chord point of the i^{th} airfoil blade on the secondary wing. And the x axis of coordinate $o_i e_x e_y e_z$ is perpendicular to the blade profile, while the y axis is coincided with the projection of the velocity of the blade quarter chord point on the blade profile. ${}^s_e R$ is rotational transformation matrix from the shoulder joint coordinate system $o_s e_x e_y e_z$ to the elbow joint coordinate system $o_e e_x e_y e_z$, which is determined by the secondary wing fixed angle ψ and elbow twist angle δ. ${}^e_j R$ is the rotational transformation matrix from the elbow joint coordinate system $o_e e_x e_y e_z$ to the local wind coordinate system $o_j e_x e_y e_z$ on the quarter chord point of the j^{th} airfoil blade on the primary wing. ${}^s_s r_i$ and ${}^s_s r_j$ are the position vectors of quarter chord point of the i^{th} airfoil blade on the secondary wing and j^{th} airfoil blade on the primary wing in the shoulder joint coordinate system $o_s e_x e_y e_z$ respectively. And ${}^s_s r_c$ is the position vector of the wing mass center in the shoulder joint coordinate system. These coordinates are illustrated in Fig. 6.

Besides, during the simulating calculation, the effects of the inertia variations caused by the deformations of primary wings is not considered due to the low mass ratio of the primary wings. In this case, the twist motions of the primary wings can be decoupled from the whole-body dynamic motion, which can be considered as two linear subsystems, and equations of these subsystems are expressed as:

$$J\ddot{\delta} + C\dot{\delta} + K\delta = \tau \tag{11}$$

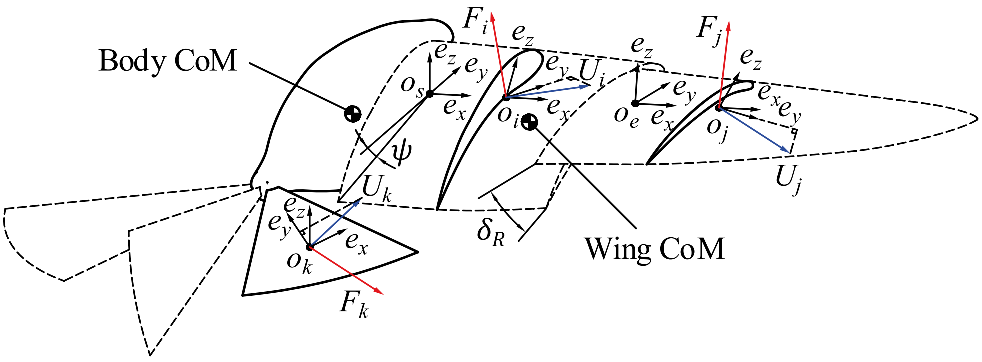

Fig. 6 Aerodynamic force on wing blades and tail fans

Where, J is the moment of inertia of the primary wing about its elbow joint, C and K are the damping coefficient and stiffness coefficient respectively, these two parameters can be obtained by the system identification experiment which is shown at physical prototype part in this work. τ is the external torque acts on each elbow joint caused by both the aerodynamic load on corresponding primary wing and the gravitational force, and it can be obtained as Eq. 12, in which ${}^e_e j$ is the position vector of the quarter chord point of the j^{th} airfoil blade of the primary wing in the elbow joint coordinate system $o_e e_x e_y e_z$. ${}^e_e r_c$ is the position vector of the primary wing mass center in the elbow joint coordinate system. ${}^O_e R$ is the rotational transformation matrix from the global coordinate system to the elbow joint coordinate system. And m_p is the mass of the primary wing.

$$\tau = [1\ 0\ 0]\cdot\left[\sum {}^e_e r_j \times \left({}^e_j R \cdot \begin{bmatrix} 0 \\ -dF_D(t,r)_j \\ dF_L(t,r)_j \end{bmatrix}\right) + {}^e_e r_c \times \left({}^O_e R^{-1} \cdot \begin{bmatrix} 0 \\ 0 \\ -m_p g \end{bmatrix}\right)\right] \tag{12}$$

The same method is adopted to obtained the aerodynamic loads on the tail fans, in which the distributed aerodynamic loads are equivalent to the concentrated force on the aerodynamic center of each tail fans. As shown in Fig. 6, the wind coordinate of each tail fan is located on the fan aerodynamic center, whose x axis is perpendicular to the longitudinal symmetry plane of the tail fan, while the y axis which locates on the longitudinal symmetry plane of tail fan is coincided with the projection of the velocity of the tail fan aerodynamic center on the longitudinal symmetry plane of the tail fan. After that, the z axis of the wind coordinate can be determined by the right-hand rule. Besides, the effect of the lateral component of the airflow on each tail fan is neglected due to the thin airfoil of tail fans. In this case, the aerodynamic force and moment on the vehicle body caused by three tail fans in the body coordinate system can be expressed as:

$$\begin{aligned} {}^B_B f_{ext} &= \sum {}^B_T R_k \cdot \begin{bmatrix} 0 \\ -dF_{Dk} \\ dF_{Lk} \end{bmatrix} \\ {}^B_B n_{ext} &= \sum {}^B_B r_k \times \left({}^B_T R_k \cdot \begin{bmatrix} 0 \\ -dF_{Dk} \\ dF_{Lk} \end{bmatrix}\right) \end{aligned} \tag{13}$$

In which, ${}^B_T R_k$ is the rotational transformation matrix from the vehicle body-fixed coordinate $o_B e_x e_y e_z$ to the wind coordinate of the k^{th} tail fan. And the lift F_L and drag F_D of each tail fan can be calculated as Eq. 14 in which C_{Lk} and C_{Dk} are the lift coefficient and drag coefficient of the k^{th} tail fan respectively, S_k is the area of the k^{th} tail fan, and $\bar{U}_k$ is the componment of the velocity of the k^{th} tail fan aerodynamic center on the longitudinal symmetry plane of the tail fan.

$$\begin{aligned} F_{Lk} &= \tfrac{1}{2} C_{Lk} \rho S_k \bar{U}_k^2 \\ F_{Dk} &= \tfrac{1}{2} C_{Dk} \rho S_k \bar{U}_k^2 \end{aligned} \tag{14}$$

2.5 Flight Dynamic Simulator Architecture

The simulator architecture shown in Fig. 7 consists of five parts including actuator part, aerodynamics module, multi-body dynamic module, primary wings passive twist dynamic module and controller part. In which, actuator part made up of wing actuator whose function is generating the motions of two shoulder joints according to the time and tail actuators which can translate the control signal into the rotational motions of the tails fans and limit the deflect angle of each tail fan into [– 45°, 45°]. According to the motion signals of the wings, vehicle body and tails, the aerodynamic module can generate the signals of aerodynamic forces. The input signals of the primary wings passive twist dynamic module are the torques on the elbow joints caused by the aerodynamic loads on the primary wings, and the output signals of this module are the twist motions of primary wings. The multi-body dynamic module can simulate the evolution of the vehicle based on the wing kinematic signals and aerodynamic forces. And the function of the controller part is sampling the motion signals of vehicle body and generating the control signals to the tail actuators.

This flapping-wing aerial vehicle flight system is a nonautonomous system, since the variation of system state depends on the time. And the motion equations of this system can be reformed as:

$$\dot{x} = f(x, t) \tag{15}$$

In which, $x = [p_x, p_y, p_z, q_x, q_y, q_z, \dot{p}_x, \dot{p}_y, \dot{p}_z, \dot{q}_x, \dot{q}_y, \dot{q}_z, \delta_R, \delta_L, \dot{\delta}_R, \dot{\delta}_L]^T$ is the system state, and f is a 16 dimensional vector function. Besides, the set of the initial value of system state x_0 is necessary. The simulation environment in this work is MATLAB/SIMULINK, fixed step Runge-Kutta solver is adopted to calculation the Eq. 15, and the simulating step time is 1/6 ms, while the flapping-wing frequency is 3 Hz.

3 Flight Simulation and Stability Analysis

In this section, the longitudinal stability, later-directional stability and the stability of the vehicle prototype controlled flight are analyzed. During flight, the aerodynamic forces acted on the prototype are periodic due to the periodic motions of the wings. Hence, the Poincare map method is adopted to analyze the periodic motion of the vehicle flight, and the flight stability is also analyzed based on this method.

3.1 Poincaré Map and Stability of Periodic Motion

Poincaré map is a common method for analyzing periodic motion, which constructs a surface of section to capture the periodic orbit of system state on the fixed point. And the stability of this fixed point is equivalent to the stability of the periodic orbit [34].

If replace t with new item θ in Eq. 15, then the original nonautonomous system can be reformed as an autonomous system which is shown at Eq. 16, where, the variable $x = [p_x, p_y, p_z, q_x, q_y, q_z, \dot{p}_x, \dot{p}_y, \dot{p}_z, \dot{q}_x, \dot{q}_y, \dot{q}_z, \delta_R, \delta_L, \dot{\delta}_R, \dot{\delta}_L]^T$ is the system state vector of the vehicle flight simulating system.

$$\begin{cases} \dot{x} = f(x, \theta) \\ \dot{\theta} = 1 \end{cases} \tag{16}$$

The flow generated by this system is $\phi(t, (x, \theta)) = (x(t), \theta(t))$. If $\Sigma \subset R^{16} \times S^1$ is a hypersurface, and for any $(x, \theta) \in \Sigma$, the normal vector of Σ at this point $n(x, \theta)$ is not orthogonal to the vector field $[f(x, \theta), \dot{\theta}]^T$, that is $n(x, \theta) \cdot [f(x, \theta), \dot{\theta}]^T \neq 0$, then this hypersurface Σ can be set as the surface of section of Poincaré map of this vector field. If Γ is the orbit whose cycle time is T, Σ is the surface of section which intersects the Γ at point $(p, \theta_0) \in R^{16} \times S^1$, and the trajectory from the point (p, θ_0) returns to Σ for the first time after T. Then, according to continuity theorem, there is a neighborhood $U \in \Sigma$ of point (p, θ_0) from which the trajectory can return to the surface of section Σ. And if q belongs to U, and $\tau(q)$ is the time of the first time the trajectory returns to Σ from q, then this Poincaré map can be expressed as follow:

$$P((q, \theta_0)) = \phi(\tau(q), (q, \theta_0)) \tag{17}$$

As shown in Fig. 8, the point p fits the map $P((p, \theta_0)) = (p, \theta_0 + T)$, which makes point (p, θ_0) become a fixed point of the Poincaré map.

And let point (x_0, θ_0) be a fixed point of the Poincaré map P, for any $\varepsilon > 0$, there is a $\delta > 0$, which satisfies the condition that if $|(x, \theta_0) - (x_0, \theta_0)| < \delta$, the inequality $|P((x, \theta_0)) - (x_0, \theta_0 + \tau(x_0))| < \varepsilon$ is true, in this case, x_0 is the stable fixed point of the map.

The Poincaré map $P((x, \theta_0))$ can be expanded by Taylor Series around the fixed point (x_0, θ_0):

$$\begin{aligned} P((x, \theta_0)) = \; & P((x_0, \theta_0)) + DP((x_0, \theta_0)) \cdot (x - x_0) \\ & + O(|x - x_0|^2) \end{aligned} \tag{18}$$

In which, $DP((x_0, \theta_0))$ is the Jacobian matrix of Poincaré map $P((x, \theta_0))$ at the fixed point (x_0, θ_0). And the eigenvalues of the DP indicate the stability of fixed point. If all the eigenvalues of DP satisfy the inequality $|\lambda| \leq 1$ then the fixed point is stable. And if the condition is stricter that $|\lambda| < 1$, then the fixed point is asymptotically stable. On the contrary, if one of the eigenvalues is greater than one, then the fixed point is unstable.

For the system of Eq. 16, it is hard to find the analytical form of the state orbit and the Poincaré map. In this work, numerical method is adopted to obtain the Jacobian matrix, whose form is expressed at Eq. 19.

$$\begin{aligned} DP((x_0, \theta_0))_{ij} = \; & \frac{P((x_0 + \Delta x_j, \theta_0))_i}{2\delta x_j} \\ & - \frac{P((x_0 - \Delta x_j, \theta_0))_i}{2\delta x_j} \end{aligned} \tag{19}$$

In which, $DP((x_0, \theta_0))_{ij}$ is the element in i^{th} row and j^{th} column of the Jacobian DP, Δx_j is a column vector whose j^{th} element is δx_j while other elements are zero. $P((x_0 + \Delta x_j, \theta_0))_i$ and $P((x_0 - \Delta x_j, \theta_0))_i$ are the i^{th} elements of the state vector after a Poincaré map of $(x_0 + \Delta x_j, \theta_0)$ and $(x_0 - \Delta x_j, \theta_0)$ respectively.

3.2 Longitudinal Stability Analysis

During the analysis of the longitudinal stability, the vehicle motion is limited in a vertical plane. In this case, the later-directional motion of the vehicle is constrained, which can be expressed as $[\dot{p}_x, \ddot{p}_x, q_y, \dot{q}_y, \ddot{q}_y, q_z, \dot{q}_z, \ddot{q}_z]^T = 0$. Through simulation, the flapping-wing vehicle flight system

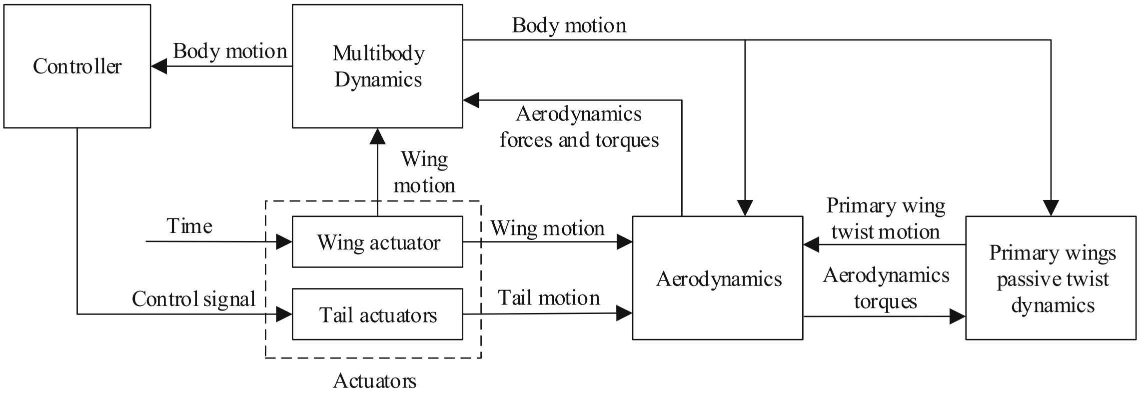

Fig. 7 Simulator architecture of the vehicle prototype

enters periodic motion orbit when the initial condition is set as Eq. 20.

$$x_0 = [0, 0, 0, -0.0843, 0, 0, 0, 4.2612, -1.2197, 0.3038, 0, 0, 0.1409, 0.1409, -4.0492, -4.0492]^T \tag{20}$$

Figure 9 shows the variation of related state of the periodic motion during two flapping wingbeats, it can be found that the pitch angle q_x fluctuates around -7°, the forward speed $\dot{p}_y$ fluctuates around 4.3 m/s, the upward speed $\dot{p}_z$ fluctuates around -1 m/s. And the state pitch angle rate $\dot{q}_x$, elbow joint angle δ and its rate $\dot{\delta}$ fluctuate around 0, while the cure of $\dot{q}_x$ has two wave crests, and the cures of δ and $\dot{\delta}$ have four wave crests.

For analyzing the stability of the longitudinal motion of the vehicle, $\Sigma = \{(x, \theta) \in R^{16} \times S^1 | \theta = kT\}(k \in N)$ is adopted as the surface of section to trim the periodic motion of the flow trajectory. During analysis, the states considered are $(q_x, \dot{p}_y, \dot{p}_z, \dot{q}_x, \delta_R, \delta_L, \dot{\delta}_R, \dot{\delta}_L)$ due to the fact that the later-directional motion related states are constrained and forward displacement p_y and upward displacement p_z are nonperiodical.

According to Eq. 19, the Jacobian matrix is expressed as Eq. 21 and its eigenvalues of the longitudinal periodical motion of the vehicle can be obtained, which is shown at Eq. 22.

$$DP = \left[\begin{matrix} 0.1729 & 0.1527 & 0.1036 & 0.0361 & 0.0089 \\ -1.1112 & 0.6383 & -0.2746 & -0.0642 & 0.1330 \\ 0.2892 & 0.7422 & 0.4318 & 0.1217 & -0.0533 \\ -1.0431 & 0.3402 & -0.1148 & -0.0692 & 0.2147 \\ -0.0445 & -0.0530 & 0.0458 & -0.0023 & -0.5816 \\ -0.0445 & -0.0530 & 0.0458 & -0.0023 & 0.0757 \\ 7.7382 & 0.0537 & -0.8962 & 0.4142 & 28.3640 \\ 7.7382 & 0.0537 & -0.8962 & 0.4142 & -7.3981 \end{matrix}\right. \\ \left.\begin{matrix} 0.0082 & 0.0000 & 0.0000 \\ 0.1340 & -0.0011 & -0.0011 \\ -0.0559 & 0.0002 & 0.0002 \\ 0.1899 & -0.0038 & -0.0037 \\ 0.0731 & -0.0122 & 0.0032 \\ 0.5843 & 0.0033 & -0.0123 \\ -7.1694 & -0.5889 & 0.0815 \\ 28.5927 & 0.0843 & -0.5918 \end{matrix}\right] \tag{21}$$

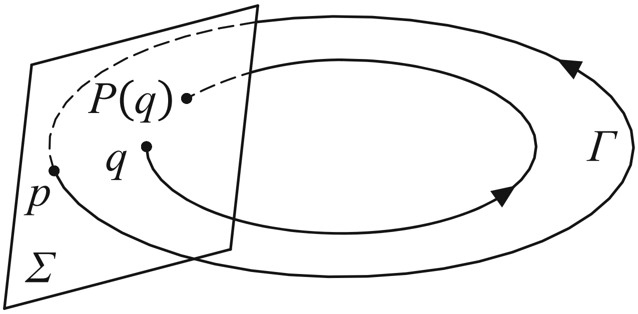

Fig. 8 Schematic of Poincaré map

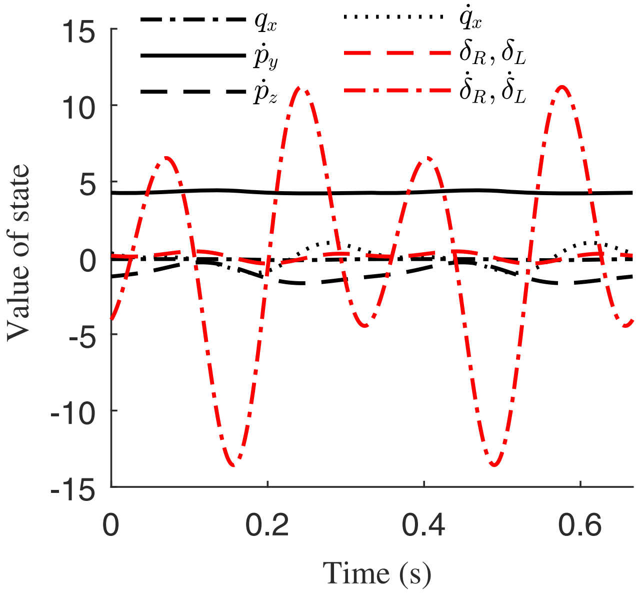

Fig. 9 Variation of state during two wingbeats

And the eigenvalues of the Jacobian matrix are:

$$\begin{aligned}\lambda = {} & 0.5664 \pm 0.6547i, -0.4953 \pm 0.4436i, \\ & 0.0078 \pm 0.0166i, -0.6653 \pm 0.7439i\end{aligned} \tag{22}$$

Hence, the longitudinal periodical motion of the prototype is asymptotically stable.

3.3 Later-Directional Stability Analysis

When the constraint of the longitudinal plane of the vehicle flight is removed, the vehicle will fly freely with the deflection angles of elevator and rudder set to be zero. Figure 10 illustrates the trajectory of the vehicle body mass center during the uncontrolled flight under the initial conditions of Eq. 20. It can be found that the vehicle gradually deviates from the initial course after releasing, and then enters a flight state which is similar to spiral motion.

According to the flight simulation, when the initial state equals (23), the vehicle will present a periodical motion state which is similar to spiral flight.

$$\begin{aligned}x_0 = {} & [0, 0, 0, -0.0843, -0.0133, 2.1766, -3.4972, \\ & -2.4353, -1.2198, 0.3038, 0.0050, 0.0284, \\ & 0.1410, 0.1408, -4.0475, -4.0502]^T\end{aligned} \tag{23}$$

In this case, $\Sigma = \{(x, \theta) \in R^{16} \times S^1 | q_z = q_{z0} + 2k\pi\} (k \in N)$ is adopted as the surface of section to trim the periodic motion of the flow trajectory. And the periodical states considered are $(p_x, p_y, q_x, q_y, \dot{p}_x, \dot{p}_y, \dot{p}_z, \dot{q}_x, \dot{q}_y, \dot{q}_z, \delta_R, \delta_L, \dot{\delta}_R, \dot{\delta}_L)$. And according to Eq. 19, the Jacobian matrix and its eigenvalues of the uncontrolled motion of the vehicle can be obtained.

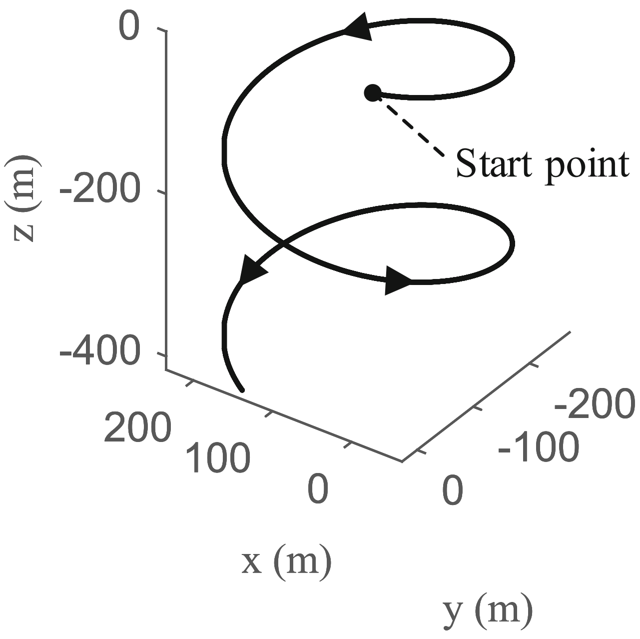

Fig. 10 Trajectory of vehicle uncontrolled flight

$$\begin{aligned}\lambda = {} & 1, 1, 0.0344, 0.0032, 7.0466 \times 10^{-4}, 1.5369 \times 10^{-8}, \\ & -4.7522 \times 10^{-9}, 2.6702 \times 10^{-9}, -3.7730 \times 10^{-13} \\ & \pm 4.1496 \times 10^{-12} i, 1.9202 \times 10^{-12}, 7.9685 \times 10^{-14}, \\ & -7.6684 \times^{-14} \pm 1.0574 \times 10^{-13} i\end{aligned} \tag{24}$$

Equation 24 lists the eigenvalues of the Jacobian matrix of the Poincaré map. There are two eigenvalues' norm equal to one while other's smaller than one, this means the periodical spiral flight is stable. In addition, if the horizontal position (p_x, p_y) is not considered, then the two eigenvalues which equal to one will be removed, in this case, other periodical states are asymptotically stable.

3.4 Stability Analysis of Close-Loop Controlled Flight

Although, the uncontrolled flight of the vehicle is stable, its yaw angle varies constantly and its pitch angle fluctuates around a certain value, which is not enough to meet the requirements of the general flight mission. For realizing the stabilization control of the pitch and yaw to desired values, two independent PID controllers were designed in pitching channel and yaw control channel respectively based on the approximate linear models.

However, the pitch and yaw data of the vehicle fluctuate constantly due to the periodical flapping wing motion, which increases the difficulty of the system identification for the two approximate linear models. In this work, sliding average filtering method is adopted to process the Euler angular data of the vehicle flight system, which can reduce the impact of the fluctuations on identification. In this case, the processed pitch and yaw angular incremental signals can be expressed as Eq. 25, where, $T = \frac{1}{3}$ s is euqal to the periodic time of one flapping wing beat.

$$\begin{aligned}\bar{\Delta} q_x(t) &= \frac{\int_{t-T}^{t} \Delta q_x(\tau) d\tau}{T} \\ \bar{\Delta} q_z(t) &= \frac{\int_{t-T}^{t} \Delta q_z(\tau) d\tau}{T}\end{aligned} \tag{25}$$

In this work, pulse signal, step signal and harmonic signal are adopted as the driving signal of elevator and rudder. According to the input signals and two processed signals $\bar{\Delta} q_x$ and $\bar{\Delta} q_z$, two approximate linear SISO systems whose transfer functions are expressed at Eq. 26 can be obtained around the stable periodic orbit of the vehicle.

$$\begin{aligned}\frac{\bar{\Delta} q_x(s)}{\delta_e(s)} &= \frac{-0.3297s^3+10.2496s^2+22.8000s-0.0563}{s^4+5.5898s^3+11.9762s^2+39.5123s+0.1153} \\ \frac{\bar{\Delta} q_z(s)}{\delta_e(s)} &= \frac{0.0226s+1.0391}{s^2+0.0454s+0.0373}\end{aligned} \tag{26}$$

For elevator deflection – incremental pitch angle system, a PID controller whose $P = 1$, $I = 0.5$, $D = 0.3$ and control period is 20 ms is adopted as the feedback controller of this subsystem. And for the rudder deflection – incremental yaw angle system, the other PID controller whose $P = 0.3$, $I = 0.02$, $D = 0.5$ and control period is 20 ms is adopted as the feedback controller of this subsystem.

Figure 11 shows the responses of real vehicle flight model and its approximate linearized model to the step signal. It can be found that the cures of the linearized model output signals can indicate the variations of the real model response. However, compared with the pitch channel, there are still some deviations between the output signals of the linearized rudder deflection – incremental yaw angle system and the real vehicle system.

The analysis of the controlled flight of the vehicle is still based on the Poincaré map method, while the desired pitch and yaw are set to be 0° respectively. According to simulation, the vehicle will enter a periodical orbit under the initial conditions expressed as Eq. 27.

$$\begin{aligned} x_0 = {} & [0, 0, 0, 0.0241, 1.6549 \times 10^{-4}, 3.3399 \times 10^{-5}, \\ & 6.9085 \times 10^{-4}, 3.7434, -1.3251, 0.4694, \\ & -0.0038, 1.3781 \times 10^{-4}, 0.1450, 0.1456, \\ & -4.1926, -4.1767]^T \end{aligned} \tag{27}$$

In this case, $\Sigma = \{(x, \theta) \in R^{16} \times S^1 | q_z = 0\}$ is adopted as the surface of section to trim the periodic motion of the flow trajectory. And the periodical states considered are $(p_x, p_y, q_x, q_y, \dot{p}_x, \dot{p}_y, \dot{p}_z, \dot{q}_x, \dot{q}_y, \dot{q}_z, \delta_R, \delta_L, \dot{\delta}_R, \dot{\delta}_L)$. According to Eq. 19, the Jacobian matrix and its eigenvalues of the uncontrolled motion of the vehicle can be obtained.

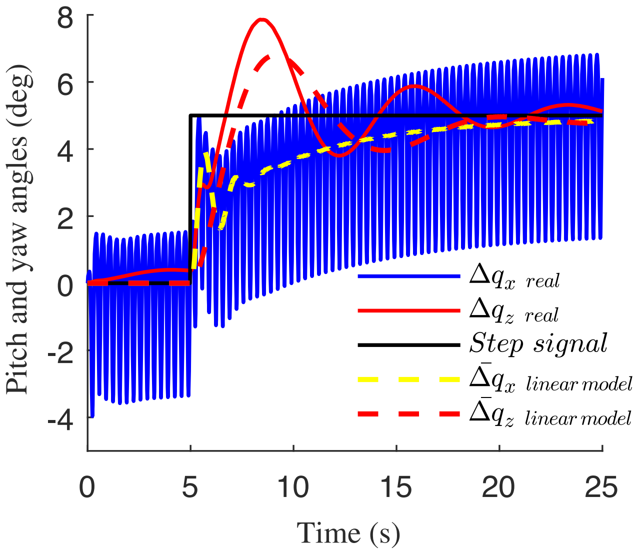

Fig. 11 Responses of the models to the step signal

$$\begin{aligned} \lambda = {} & 1, 1, -0.8028, -0.4172, -0.1937, -0.2157 \\ & \pm 0.1262i, -0.0696 \pm 0.1897i, 0.0637, 0.0011, \\ & -0.0022 \pm 0.0006i \end{aligned} \tag{28}$$

Equation 28 lists eigenvalues of the Jacobian matrix of the Poincaré map. There are two eigenvalues' norm equal to one while other's smaller than one, which indicates that the controlled flight of the vehicle is stable. What's more, if the horizontal position (p_x, p_y) is not considered, then the two eigenvalues which equal to one will be removed, in this case, other periodical states are asymptotically stable.

4 Physical Prototype Experiments

This section shows some experiments of the physical prototype, first the flapping wing movements were recorded for the parameter identification of the passive twist of the primary wings. After that, untethered flight of the vehicle prototype under uncontrolled and controlled conditions were taken to verify the stability of the prototype.

4.1 Parameter Identification

During the parameter identification of the passive twist of the primary wings model, the wing motion of the vehicle prototype under different flapping wing frequencies was recorded by two high speed cameras which is located in front and side of the prototype respectively. After that, these videos were used to measure the wing-stroke angle and the deformation of the primary wings, in which, the wing-stroke angle can be regarded as the projected angle of the secondary wing leading edge in the front view, and the deformation of the primary wing can be indicated from the projected angle of its middle support bar which is highlighted by red lines in the side view in Fig. 12. In this case, the deformation of the primary wing will be also represented by the equivalent rotation of the primary wing around the elbow joint, which can be derived by the two projected angles data.

The kinematic data of the wings under three flapping wing frequencies including 1 Hz, 2.9 Hz and 5 Hz was obtained in the identification experiments. Figure 13 illustrates the wing-stroke angle data at three flapping wing frequencies, it can be found that the experimental data expressed by the realistic lines are approximately consistent with the designed wing flapping motion rule represented by the dashed line, which verifies the feasibility of the flapping wing mechanism.

For identifying the parameters including equivalent moment of inertial J, rotational damping C and rotational

Fig. 12 Morphological variation of wings during 2.9 Hz flapping

stiffness K of the passive twist model of primary wings, the least square method is adopted to evaluate the differences between the output signals of the mathematical model under body fixed condition and the experimental data, whose expression is listed at Eq. 29.

$$f = \sum [\delta_{experiment}(i) - \delta_{model}(i)]^2 \tag{29}$$

In which, the equivalent passive rotation of primary wings at physical experiments $\delta_{experiment}$ is derived by the projected angle of middle support bar of the primary wing in the side view which is expressed in Eq. 30. Where, $\theta_{experiment}(i)$ is the projected angle of middle support bar on the side view of the i^{th} frame, $\phi_{experiment}(i)$ is the wing-stroke angle in the i^{th} frame. ${}^{O}_{S}R$ is the rotation matrix from the measuring coordinate system to the secondary wing fixed coordinate system, ${}^{S}_{E}R$ is the rotation matrix from the secondary wing fixed coordinate system to the primary wing fixed coordinate system, and E_{bar} is orientation cosine vector of middle support bar in the primary wing fixed coordinate system. And the equivalent passive rotation of

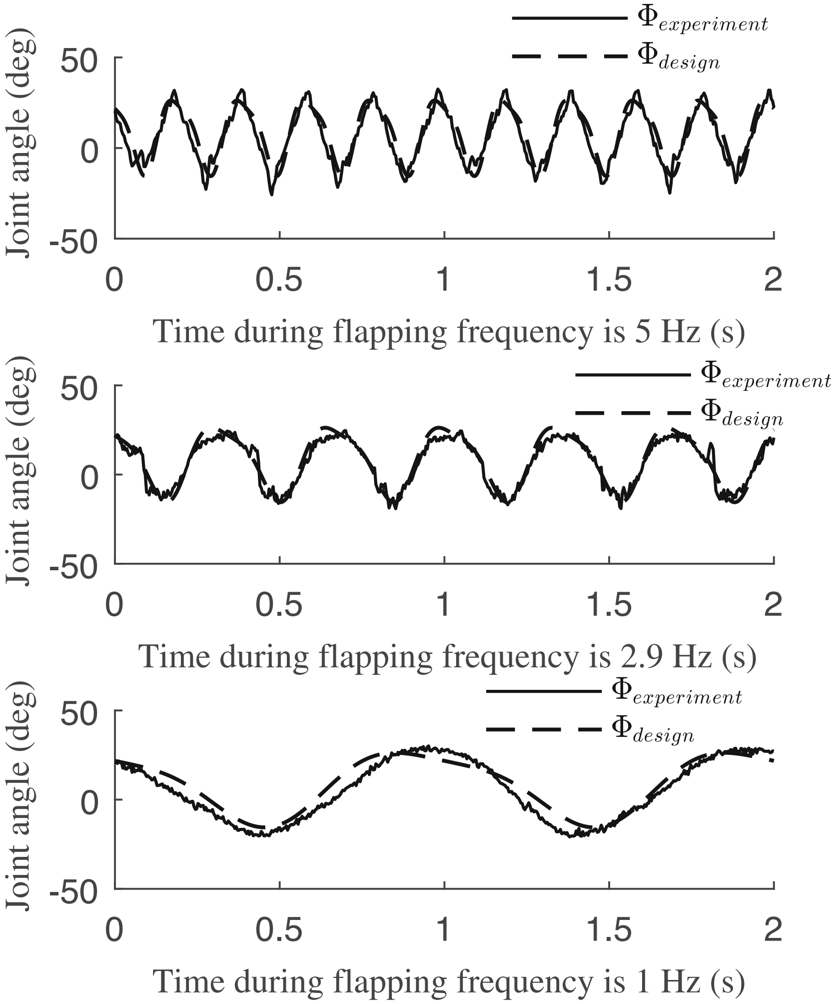

Fig. 13 Shoulder joint angle of different flapping frequency

the primary wing $\delta_{experiment}$ can be obtained by solving the nonlinear equation of Eq. 30.

$$\begin{bmatrix} 0 \\ cos(\theta_{experiment}(i)) \\ sin(\theta_{experiment}(i)) \end{bmatrix} = {}^{O}_{S}R(\phi_{experiment}(i)) \cdot {}^{S}_{E}R(\delta_{experiment}(i)) \cdot E_{bar} \tag{30}$$

$$\begin{cases} min\ f(X) = \sum[\delta_{experiment}(i) - \delta_{model}(i)]^2 \\ X \in [J, C, K, \delta_0^1, \dot{\delta}_0^1, \delta_0^2, \dot{\delta}_0^2, \delta_0^3, \dot{\delta}_0^3]^T \\ S.T.\ 0 \le J \le 0.01 \\ \quad 0 \le C \le 0.2 \\ \quad 1 \le K \le 4 \\ \quad -40^\circ \le \delta_0^j \le 40^\circ \\ \quad -1 \le \dot{\delta}_0^j \le 1 \end{cases} \tag{31}$$

In order to minimize the difference between the simulation model and the real model, particle swarm optimization algorithm is used in this work to optimize the least squares value of Eq. 29, so as to obtain the relevant parameters of the passive twist model of the primary wing. And this optimization problem can be expressed as Eq. 31, in which δ_0^j and $\dot{\delta}_0^j$ are the initial twist angle and twist angular velocity of the primary wing respectively.

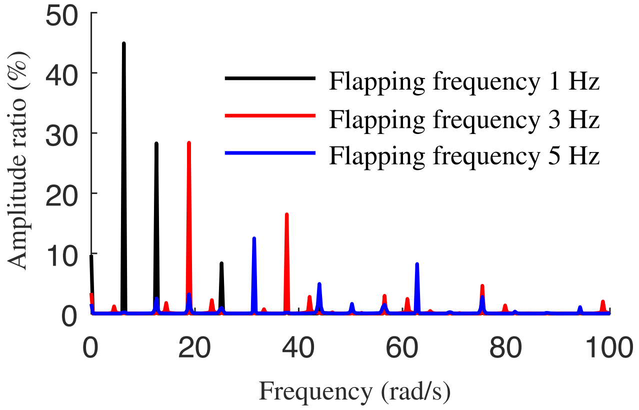

Fig. 15 Spectral distribution of torques act on elbow joint

Fig. 14 Elbow joint angle of different flapping frequency

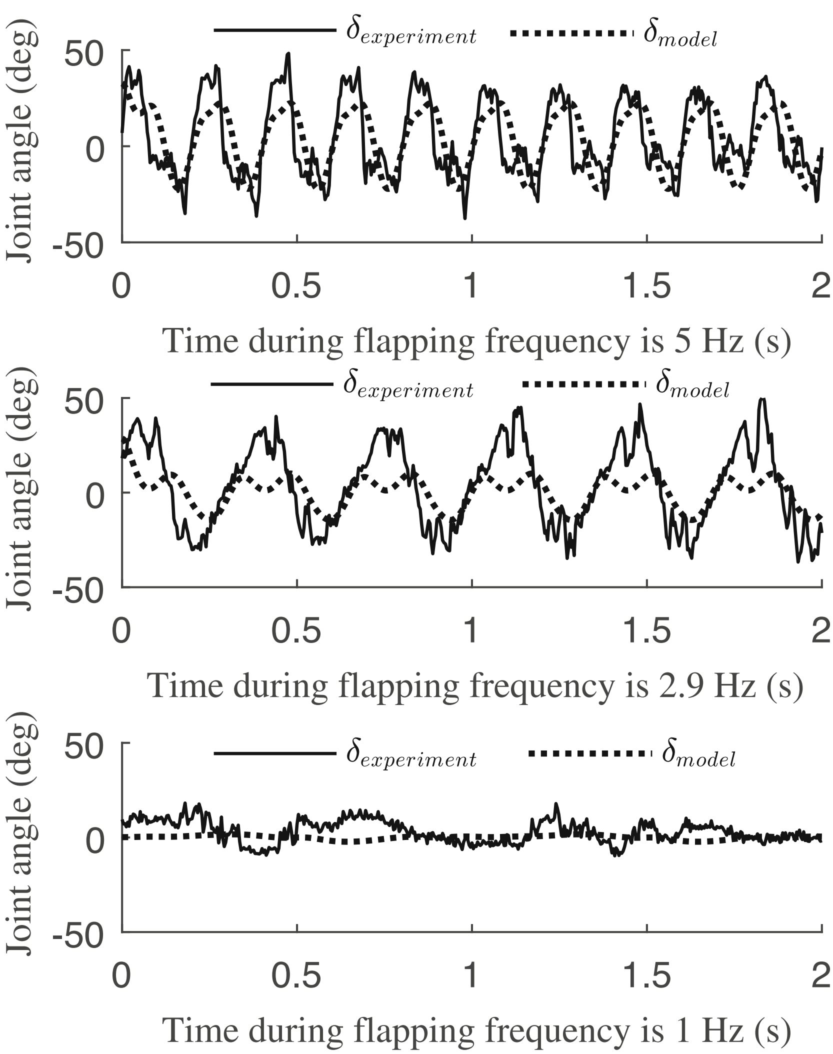

Fig. 16 Motion Sequence of the Vehicle Uncontrolled Flight

Through iterative optimization, the three parameters of the passive twist model can be obtained: $J = 0.0021\,\mathrm{kg \cdot m^2}$, $C = 2.5 \times 10^{-5}\,\mathrm{N \cdot s \cdot m^{-1}}$, $K = 3.5780\mathrm{N \cdot m^{-1}}$. Figure 13 illustrates the shoulder joint angle of vehicle at different flapping frequencies including 1 Hz, 2.9 Hz and 5 Hz, the experiment results show that the should joint movement can realize the predetermined motion rule expressed at Eq. 1. And, Fig. 14 illustrates the comparison of the equivalent elbow rotation data between simulation model and the physical prototype under three different flapping wing frequencies. It can be found the simulation data represented by the dashed line can basically reflect the motion trend of the equivalent elbow twist of prototype primary wing. However, there are some differences between the simulation data and experiment results, which may be caused by measurement error.

In addition, the inherent frequency of the identified second-order linear system shown in Eq. 11 is determined at around 40 rad/s after linear analysis. Figure 15 illustrates the frequency distribution of torques act on elbow joint at different flapping wing frequencies. It can be found that the fundamental component of torque signal at 3 Hz flapping wing frequency locates near to the inherent frequency of the twist system. Based on this property, the vibration amplitude of primary twist motion is sensitive to the flapping wing frequency near 3 Hz, which causes the obvious difference between the experiment and simulation results in Fig. 14 when the frequency is 2.9 Hz. What's more, the modeling error between the equivalent linear model and the physical model also made a contribution to this difference. In this work, the structural deformation of the primary wing is approximately substituted by its second-order linear rigid rotational motion to speed up the vehicle flight dynamic calculation. However, this method will induce the modeling error between equivalent model and physical model. As a result, this modeling error could be magnified when the flapping wing frequency near to the structural resonance frequency of the primary wing.

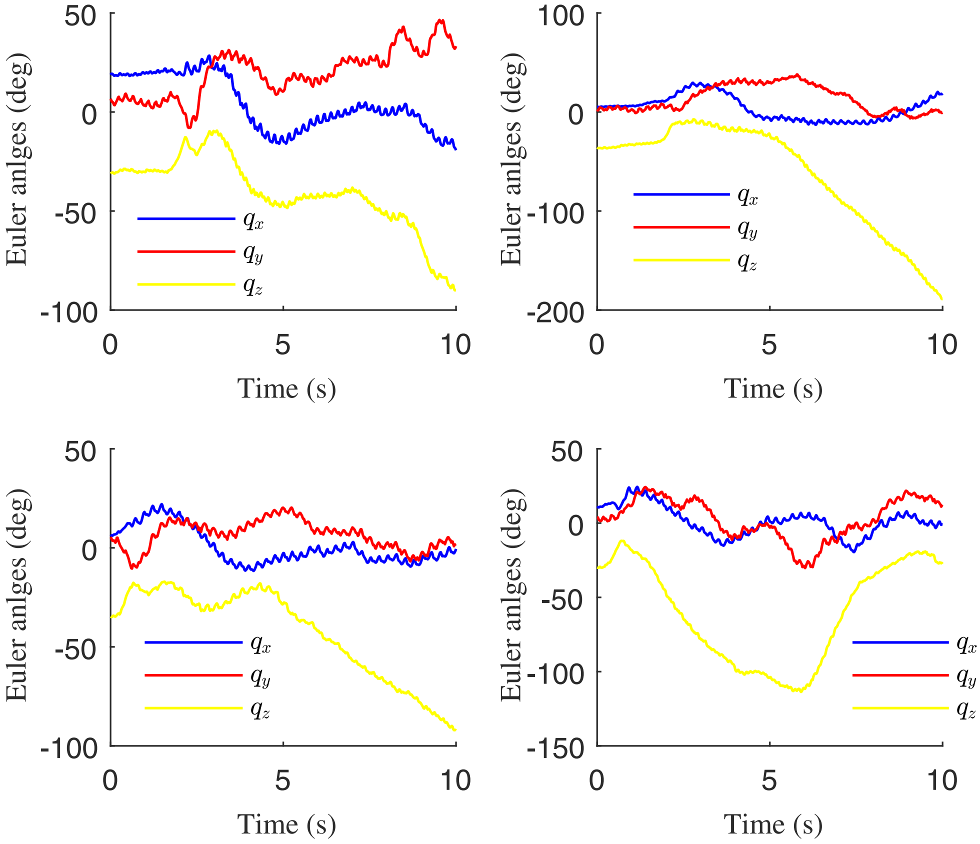

Fig. 17 Euler angles of four tests of uncontrolled flight

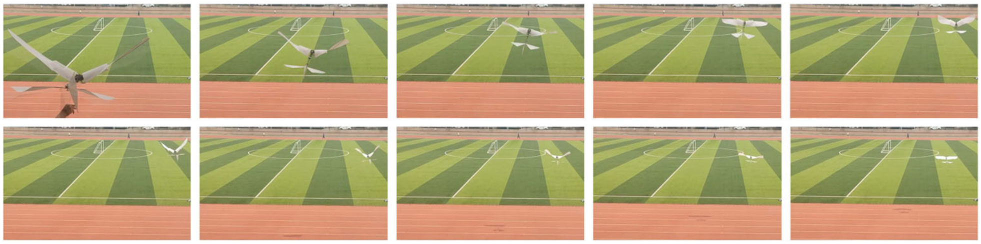

Fig. 18 Motion sequence of the vehicle controlled flight

4.2 Uncontrolled Flight Experiment

For verifying the stability of vehicle prototype under uncontrolled condition, the untethered flight experiment of the prototype was carried out outdoors, which is illustrated in Fig. 16 as the form of motion sequence. During the flight experiment, the deflect angles of elevator and rudder were set to be 0° respectively. As shown in Fig. 16, the course of the prototype will gradually deviate from the initial flight direction in the early stage of flight, and then, the prototype will enter a spiral like flight state in the later stage.

Figure 17 illustrates the variation of the Euler angles of the prototype during four uncontrolled flight tests. As shown in Fig. 17, the pitch angle q_x represented by the blue lines moves to the vicinity of 0° and vibrates periodically around 0° , while the roll angle q_y represented by the red lines varies to the upside of 0° and then fluctuates within that range. However, the yaw angle q_z represented by the yellow lines can not be stabilized near a fixed value, instead, it will move towards the negative direction, which indicates that the vehicle prototype presents a flight state which is similar to spiral flight.

4.3 Controlled Flight Experiment

Figure 18 illustrates the motion sequence of the controlled flight of the vehicle prototype, in which, the desired pitch angle is set as $q_x = 0°$, and the desired yaw angle is set as $q_z = 0°$. The motion sequence of Fig. 18 indicates that the vehicle prototype can stabilize the yaw angle, however, the

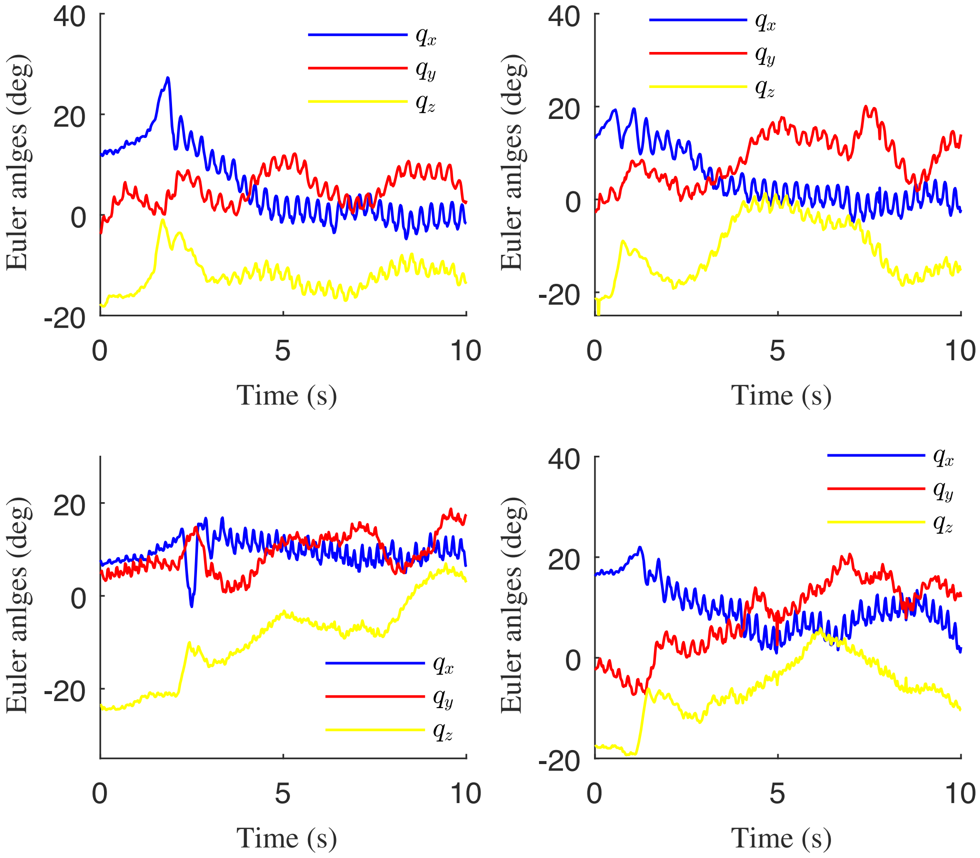

Fig. 19 Euler angles of four tests of controlled flight

prototype still has a lateral displacement during controlled flight.

Figure 19 illustrates the variation of the Euler angles of the prototype during four controlled flight tests. It can be found that the pitch angle q_x is stable to the vicinity of 0° and vibrates periodically around 0° , while the roll angle q_y and the yaw angle q_z stabilize to the vicinity of 10° and -10° respectively, which verifies the stability of the prototype under controlled flight conditions. However, there are still some differences between the roll angle and yaw angle data of the physical prototype and the simulation results, which may be leaded by the difference in the movement and deformation of the wings on both sides caused by the manufacturing error of the physical prototype. In this case, the positive roll angle and the negative angle make the prototype have the tendency to move to the side direction, which explains the displacement in the lateral direction of the physical prototype in Fig. 18.

5 Conclusions and Future Work

In this paper, the mathematic model which considers the impact of the deformations of the wings is established for a flapping-wing vehicle. Based on this model, the longitudinal and later-directional stability of prototype uncontrolled flight are proved to be steady combined with the untethered flight experiment. After that, for preventing the stable spiral-like flight in prototype uncontrolled flight, two independent PID controllers are designed based on the approximate linear model in the vicinity of the equilibrium flight condition. And the controlled flight of the prototype is also proved to be stable based on the mathematic model and untethered flight experiment.

As a continuation of this work, a more complete controller which considers the position close-loop and resistance to disturbance need to be designed, which will improve the capacity and performance of the flapping-wing vehicle prototype.

Acknowledgements This research work was supported by the National Key Research and Development Program of China under Grant 2017YFB1300101.

Author Contributions All authors contributed to the study conception and design. Material preparation, data collection and analysis were performed by Yaolei Shen and Pu Miao. The first draft of the manuscript was written by Yaolei Shen and all authors commented on previous versions of the manuscript. All authors read and approved the final manuscript.

Funding This research work was funded by the National Key Research and Development Program of China under Grant 2017YFB1300101.

Availability of data and material The datasets used or analysed during the current study are available from the corresponding author on reasonable request.

Code Availability The raw/processed data required to reproduce these findings cannot be shared at this time as the data also forms part of an ongoing study.

Declarations

This research work did not involve humans participants or animals. Hence, **ethics approval**, **Consent to participate** and **Consent for publication** are not applicable.

Conflict of Interests The authors declare that they have no conflict of interest.

References

1. Shyy, W., Aono, H., Kang, C.K., et al.: An Introduction to Flapping Wing Aerodynamics. Cambridge University Press, Cambridge (2013)
2. Wood, R.J.: The first takeoff of a biologically inspired at-scale robotic insect. IEEE Trans. Robot. **24**(2), 341–347 (2008)
3. De Croon, G.CHE., Perçin, M., Remes, B., Ruijsink, R., De Wagter, C.: The DelFly: design, aerodynamics, and artificial intelligence of a flapping wing robot. Springer Publishing Company Incorporated (2015)
4. Keennon, M., Klingebiel, K., Won, H.: Development of the nano hummingbird: a tailless flapping wing micro air vehicle. In: 50th AIAA Aerospace Sciences Meeting including the New Horizons Forum and Aerospace Exposition (2012)
5. Gerdes, J., Holness, A., Perez-Rosado, A., et al.: Robo raven: a flapping-wing air vehicle with highly compliant and independently controlled wings. Soft Robotics **1**(4), 275–288 (2014)
6. Send, W., Fischer, M., Jebens, K., et al.: Artificial hinged-wing bird with active torsion and partially linear kinematics. In: 28th International congress of the aeronautical sciences (2012)
7. Ramezani, A., Shi, X., Chung, S.J., et al.: Bat Bot (B2), a biologically inspired flying machine. In: 2016 IEEE international conference on robotics & automation, 3219–3226 (2016)
8. Shyy, W., Kang, C.K., Chirarattananon, P., et al.: Aerodynamics, sensing and control of insect-scale flapping-wing flight. Proceedings Mathematical Physical & Engineering Sciences **472**, 20150712 (2016)
9. Bulka, E., Nahon, M.: Automatic control for aerobatic maneuvering of agile fixed-wing UAVs. J. Intell. Robot. Sys. **93**, 85–100 (2019)
10. Mendoza-Mendoza, J., Gonzalez-Villela, V.J., Aguilar-Ibanez, C., et al.: Snake aerial manipulators: a review. IEEE Access **8**, 28222–28241 (2020)
11. Orlowski, C.T., Girard, A.R.: Dynamics, stability, and control analyses of flapping wing micro-air vehicles. Progress in Aerospace Sciences **51**, 18–30 (2012)
12. Taha, H.E., Hajj, M.R., Nayfeh, A.H.: Flight dynamics and control of flapping-wing MAVs: a review. Nonlinear Dynamics **70**(2), 907–939 (2012)
13. Etkin, B., Teichmann, T.: Dynamics of Flight: Stability and Control. Wiley (1982)
14. Khan, Z., Agrawal, S.: Modeling and simulation of flapping wing micro air vehicles. In: 2005 ASME International Design Engineering Technical Conferences (2005)
15. Duan, H., Li, Q.: Dynamic model and attitude control of flapping wing micro aerial vehicle. In: 2009 IEEE International Conference on Robotics and Biomimetics, pp. 451–456 (2009)
16. Lasek, M., Sibilski, K.: Modelling and simulation of flapping wing control for a micromechanical flying insect (entomopter).

In: AIAA Modeling and Simulation Technologies Conference and Exhibit (2002)

17. Grauer, J.A., Hubbard, J.E.: Multibody model of an ornithopter. J. Guid. Control Dyn. **32**(5), 1675–1679 (2009)
18. Orlowski, C.T., Girard, A.R.: Modeling and simulation of nonlinear dynamics of flapping wing micro air vehicles. AIAA J. **49**(5), 969–981 (2011)
19. Pfeiffer, A., Lee, J., Han, J., et al.: Ornithropter flight simulation based on flexible multi-body dynamics. J. Bionic Eng. **7**, 102–111 (2010)
20. Taylor, G.K., Thomas, A.L.R.: Dynamic flight stability in the desert locust Schistocerca gregaria. J. Exp. Biol. **206**(16), 2803–2809 (2003)
21. Sun, M., Xiong, Y.: Dynamic flight stability of a hovering bumblebee. J. Exp. Biol. **208**, 447–459 (2005)
22. Bolender, M.: Open-loop stability of flapping flight in hover. In: AIAA Guidance, Navigation, and Control Conference (2010)
23. Dietl, J.M., Garcia, E.: Stability in Ornithopter Longitudinal Flight Dynamics. J. Guid. Control Dyn. **31**(4), 1157–1162 (2008)
24. Lee, J.S., Kim, J.K., Kim, D.K., et al.: Longitudinal Flight Dynamics of Bio-Inspired Ornithopter Considering Fluid-Structure Interaction. J. Guid. Control Dyn. **34**(3), 667–677 (2011)
25. Kim, J.K., Lee, J.S., Han, J.H.: Passive Longitudinal Stability in Ornithopter Flight. J. Guid. Control Dyn. **35**(2), 669–674 (2012)
26. Stanford, B., Beran, P., Patil, M.: Optimal Flapping-Wing Vehicle Dynamics via Floquet Multiplier Sensitivities. J. Guid. Control Dyn. **36**(2), 454–466 (2013)
27. Bhatia, M., Patil, M., Woolsey, C., et al.: Stabilization of Flapping-Wing Micro-Air Vehicles in Gust Environments. J. Guid. Control Dyn. **37**(2), 592–607 (2014)
28. Liu, T., Kuykendoll, K., Rhew, R., et al.: Avian wing geometry and kinematics. AIAA J. **44**(5), 954–963 (2006)
29. Ramamurti, R., Sandberg, W.C.: A three-dimensional computational study of the aerodynamic mechanisms of insect flight. J. Exp. Biol. **205**, 1507–1518 (2002)
30. Sun, M.: Lift and power requirements of hovering flight in Drosophilavirilis. J. Exp. Biol. **205**(16), 2413–2427 (2002)
31. Dickinson, M.H., Lehmann, F.O., Sane, S.P.: Wing rotation and the aerodynamics basis of insect flight. Science **248**(5422), 1954–1960 (1999)
32. Willmott, A.P., Ellington, C.P., Thomas, A.L.R.: Flow visualization and unsteady aerodynamics in the flight of the hawkmoth, Manduca sexta. Philosophical Transactions of the Royal Society B: Biological Sciences **352**, 303–316 (1997)
33. Deng, X., Schenato, L., Wu, W.C., et al.: Flapping flight for biomimetic robotic insects: Part I - System modeling. IEEE Trans. Robot. **22**(4), 776–788 (2006)
34. Strogatz, S.H.: Nonlinear Dynamics and Chaos: With Applications to Physics, Biology, Chemistry, and Engineering. Westview Press (2015)

Yaolei Shen received the B.Eng. degree in Mechanical Engineering from Northwestern Polytechnical University, Xi'an, China, in 2019, with a thesis on aerial robotics. Currently, he is a master student at Northwestern Polytechnical University. His main research topics include the design and control of aerial robots.

Wenjie Ge received Ph.D. degree in Mechanical Engineering from Northwestern Polytechnical University, Xi'an, China, in 2006. He is currently a full professor in the department of Mechanical Engineering and Automation at Northwestern Polytechnical University. He is also the principal of national teaching team of basic mechanical course of China. His main research interests include bionic robotics and topology optimization for flexible wings.

Pu Miao received the B.Eng. degree in Mechanical Engineering from Northwestern Polytechnical University, Xi'an, China, in 2019, with a thesis on transmission system design of ships. Currently, he is a master student in Transmissions and Controls Lab at Northwestern Polytechnical University. His main research interests include the design and optimization of transmission system.